ACS OMEGA

http://pubs.acs.org/journal/acsodf

Article

Novel Phosphate Conversion Coating with Superior Corrosion Resistance on the Mg-Al-RE Alloy Based on the Introduction of Silane

Yongjun Zhang* and Haoyu Wang

Cite This: *ACS Omega* 2023, 8, 29374−29387

Read Online

ACCESS | Metrics & More | Article Recommendations

ABSTRACT: A novel chemical conversion method based on an aqueous electrolyte solution containing hydrolyzed silane as a crucial film-forming agent has been developed successfully. An organic/inorganic composite coating with superior corrosion protection was fabricated on the Mg-Al-RE alloy. The micro-morphology and chemical composition of the coating were examined using scanning electron microscopy, X-ray diffraction, and energy-dispersive X-ray spectroscopy. The prepared conversion coating possesses a double-layer structure, with a dense bottom layer and a loose outer layer containing microcracks. In addition, the anti-corrosion capacity of various samples was evaluated using salt spray, hydrogen evolution, and electrochemical tests. The analysis revealed that the samples converted by 3-aminopropyl triethoxysilane (APTES)-phosphate solution possessed a higher corrosion resistance. Compared to the blank sample, a 2 orders of magnitude reduction in i_{corr} (6.678×10^{-7} A/cm^2) and a 1.360 V improvement in E_{corr} were observed. The MPCC-Si sample exhibited the lowest hydrogen evolution rate, indicating the best corrosion protection. Also, the rust grade could still reach 7 after 72 h of the neutral salt spray test.

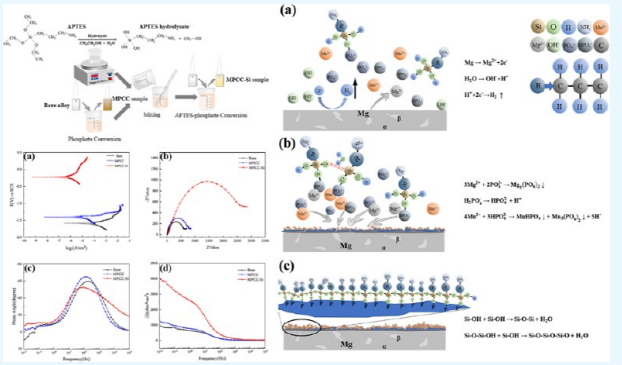

1. INTRODUCTION

Recently, researchers have investigated lightweight structural materials with excellent processing and application performance to achieve energy conservation and emission reduction goals and avoid related environmental pollution problems.[1] Mg and its alloys are preferred because of their lower density among metallic construction materials and superior mechanical properties.[2] In addition, they have specific stiffness, good castability, high thermal conductivity, low sensitivity to intergranular corrosion and stress corrosion, and low environmental pollution.[3] As a result, Mg alloys are widely used in engineering applications, such as those in aerospace, automotive manufacturing, electronic products, and defense industries.[4,5]

Rare earth elements have been added to Mg alloys to promote their various properties and expand their applications.[6−8] However, the standard electrode potential of Mg (−2.363 V) is relatively lower than that of other commonly used metals,[9] which makes it susceptible to galvanic corrosion. Due to these limitations, Mg alloys are more likely to fail when used as structural components in demanding service environments. To address this issue, various modification technologies have been developed to control the corrosion of Mg alloys, including chemical conversion,[10] electroless plating,[11] electroplating,[12] organic coating,[13] laser surface melting,[14] sol−gel,[15] microarc oxidization,[16] and high-pulsed electron beam treatment.[17] Among these technologies, chemical conversion has been widely used due to its higher protective efficacy, lower cost, and easier operation.[18,19]

Due to the unique self-healing ability of the chromium-containing coating, it is considered the best conversion coating for corrosion prevention.[20] However, chromium salts have been severely restricted due to their carcinogenicity to humans and Cr (VI)'s continuous contribution to environmental pollution.[21] Over the past decades, studies on alternatives to chromate coating have led to the proliferation of phosphate,[22] vanadium,[23] phosphate-permanganate,[24] stannate,[25] hydrotalcite,[26] rare earth,[27] titanate,[28] zirconium,[29] phytic acid,[30] and chitosan[31] conversion coatings. However, due to the cracks often present in these coatings, their anti-corrosion properties are inferior to those of chromate conversion coatings.[22] Two different theories have explained the formation of these cracks. According to one theory, the shrinkage of the coating during the drying process created tensile stress, which increased with the coating thickness,

Received: April 25, 2023
Accepted: June 20, 2023
Published: August 3, 2023

https://doi.org/10.1021/acsomega.3c02824
ACS Omega 2023, 8, 29374−29387

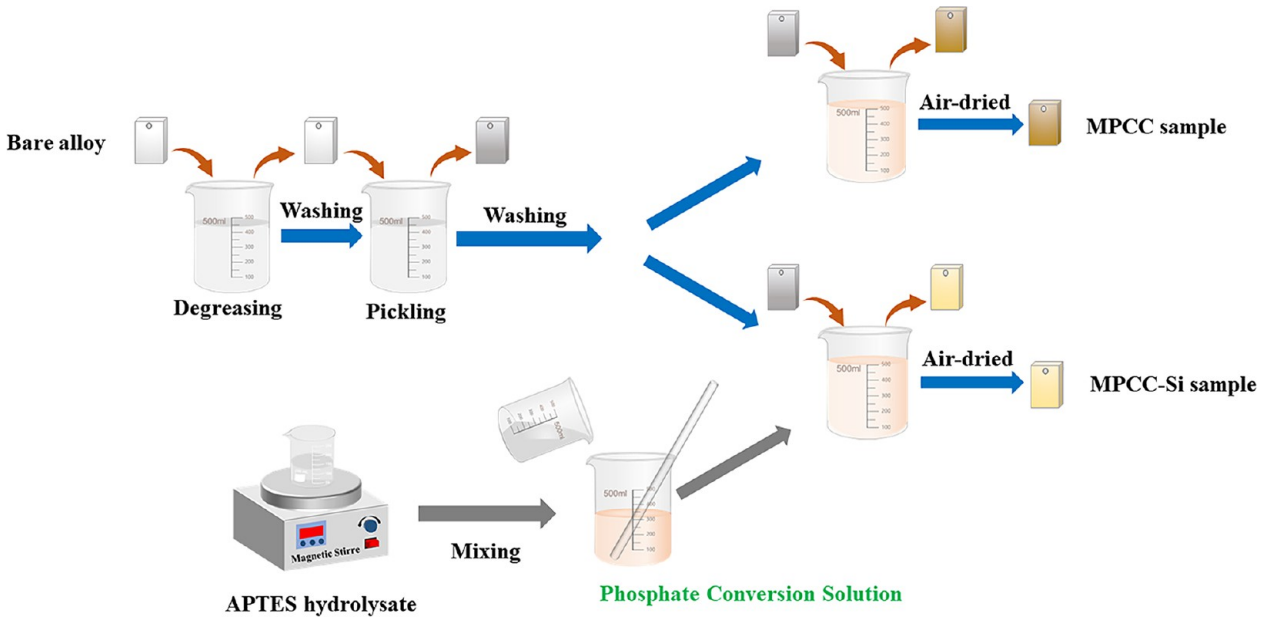

Figure 1. Schematic diagram of the preparation of chemical coatings.

and these tensile stresses will be released by coating cracking. The other theory proposes that hydrogen atoms clipped in the coating can agglomerate and combine to form bubbles, causing the coating to crack.[32] These cracks, which act as a Cl^- penetration path, are common in chromate-free conversion coatings and cause severe corrosion of Mg alloys. Therefore, a coating with no or few micro-cracks is a guarantee to achieve better corrosion resistance.

Among these conversion technologies, phosphate conversion is more environmentally friendly and has been widely used in the corrosion protection of steel, zinc, magnesium, and other metals. Phosphate coatings possess the necessary corrosion protection and other physical properties, such as biocompatibility for Ca^{2+}[33] and wear resistance for Mn^{2+}.[34] Over the past decades, the applications of Mn-PO_4,[34] Zn-PO_4,[10] Ca-PO_4,[33] and Sr-PO_4[35] conversion coatings have been successfully expanded to Mg alloys. In contrast, few researchers have focused on Mn-PO_4 conversion coating, although they are more stable and have higher corrosion resistance than Ca and Zn coatings.[36] Chen et al.[36] prepared a double-layer conversion coating consisting of magnesium hydroxide and manganese phosphate on the AZ91D alloy, and this coating exhibits good corrosion resistance. Cui et al.[37] obtained a double-layer phosphate coating on the AZ31 alloy by substituting the NaF bath with a citric bath. A new three-stage coating formation mechanism has been proposed. For the double-layer coating, the outer layer coating can fill cracks and micron holes in the inner layer, thus reducing surface and structural defects, and better preventing contact between corrosive media and the Mg alloy substrate.[38,39] Although these reported manganese-based phosphate conversion coatings possess good corrosion resistance, their coating formation times are as high as 15 min or more, which is much higher than the formation time required for industrial production.

Silanes are organic−inorganic materials polymerized from a silicon group with the formula $R'(CH_2)_nSi(OR)_3$, where R′ is an organic functional group and R is a hydrolyzable alkoxy group.[40] As silanes are mixed with water, they hydrolyze to produce silanol groups (Si-OH), which attach to metal surfaces (metal-OH) by forming Si-O-metal bonds.[41] These Si-OH formed siloxane bonds (Si-O-Si) by self-cross-linking, producing an organic protective coating chemically bound to the metal.[42] However, a single silane conversion coating possesses limited corrosion protection properties and is usually used for short-term protection.[43] To improve corrosion resistance, researchers typically prepare a double-layer silane coating in two steps or add a corrosion inhibitor to the conversion solution to fabricate the coating. Using titanium sulfate as the primary ingredient, Lai et al.[44] first prepared a TiO_2 conversion coating on the zinc layer. A solution of tetraethyl orthosilicate and hexamethyldisilazane was then used to modify the coating. The final coating was a double layer consisting of an inner coating of TiO_2 and an outer coating of SiO_2 gel. Najibzad et al.[45] used varying concentrations of inhibitors dispersed in the silane solution and deposited films by dipping in an AZ31 alloy. The salt spray test (SST) revealed that the obtained self-healing coating effectively prevented the corrosion of the alloy. Lei et al.[46] created a silane-modified cerium coating on the AZ31 Mg alloy by combining a hydrolyzed silane solution with the cerium salt conversion solution.

A few current studies have investigated the addition of silane as a main film-forming agent into the conversion solution to obtain highly corrosion-resistant conversion coatings. Researchers mainly use a two-step method to prepare organic/inorganic composite coatings,[47] which is more complicated and time-consuming to fabricate. In this study, a new chemical conversion solution that consists of hydrolyzed APTES (3-aminopropyl triethoxysilane) was prepared, and by this, a highly corrosion-resistant organic/inorganic composite double-layer coating could be prepared in one step. Furthermore, the extremely short film-forming time of this coating can help considerably improve industrial production efficiency. This study aimed to investigate the morphology, composition, and electrochemical properties of the sample produced by this chemical conversion solution containing APTES.

2. EXPERIMENTAL SECTION

2.1. Materials. A new Mg-Al-RE alloy was chosen as the substrate which was provided by Shenzhen Xinshen New

https://doi.org/10.1021/acsomega.3c02824
ACS Omega 2023, 8, 29374−29387

Material Technology Co., Ltd., China, with the following composition: Al 3.07 wt %, La 1.17 wt %, Ce 2.59 wt %, other elements 2.67 wt %, and balance Mg. The samples with the size of 30 mm × 25 mm × 5 mm were cut from the ingot. The chemicals including sodium hydroxide (NaOH), trisodium phosphate (Na_3PO_4), ferric nitrate ($Fe(NO)_3$), potassium fluoride (KF), phosphoric acid (H_3PO_4), seignette salt ($NaKC_4H_4O_6$), manganese carbonate ($MnCO_3$), chromium trioxide (CrO_3), and ammonium orthophosphate ($(NH_4)_3PO_4$) were purchased from Guangzhou Chemical Reagent Factory, China. The APTES with an effective content of 99% was purchased from Shanghai Macklin Biochemical Co., Ltd, China. All of the above-mentioned chemicals were of analytical purity grade and used without further purification.

2.2. Preparation of the Conversion Coatings. Before the conversion treatment, the samples were polished with emery paper from 240 to 1000 grits, then washed with distilled water, and finally air-dried. Anhydrous ethanol, water, and APTES were mixed in the ratio of 18:2:5 by volume, and the mixture was then stirred at 25.0 ± 3 °C to hydrolyzation. After 2.0 h of hydrolysis, the hydrolyzed solution was combined with an aqueous solution containing the remaining components. The sample preparation procedure is depicted in Figure 1 and the hydrolysis process of APTES is provided in eq 1. The samples converted with the electrolyte solution containing APTES were named MPCC-Si, in which M stands for manganese, P for phosphate, CC for conversion coating, and Si for silane. The samples prepared using the conversion solution without the addition of APTES were named MPCC samples. The compositions of the conversion solution and the conversion parameters are listed in Table 1. Both conversion solutions were

Table 1. Solution Type and Conversion Parameters

solution type	composition and concentration	parameters
degreasing	$Na_3PO_4{\cdot}12H_2O$ 10.0 g/L, NaOH 90.0 g/L	80.0 ± 3 °C, 10.0 min
pickling	$Fe(NO_3)_3{\cdot}9H_2O$ 40.0 g/L, CrO_3 180.0 g/L, KF 3.5 g/L	25.0 ± 3 °C, 2.0 min
MPCC conversion	$MnCO_3$ 25.0 g/L, H_3PO_4 45.0 mL/L, $(NH_4)_3PO_4$ 5.0 g/L, $NaKC_4H_4O_6{\cdot}4H_2O$ 7.0 g/L, pH = 3.00	25.0 ± 3 °C, 2.5 min
MPCC-Si conversion	same as MPCC solution, but APTES 15.0 mL/L is added. pH = 3.00	25.0 ± 3 °C, 2.5 min

adjusted to pH = 3.00 using NaOH solution. Following the conversion process, the samples were rinsed with distilled water and then air-dried at 25.0 ± 3 °C.

$$NH_2(CH_2)_3Si(OC_2H_5)_3 + H_2O \rightarrow NH_2(CH_2)_3Si(OH)_3 + CH_3OH \quad (1)$$

2.3. Microstructure and Composition Characterizations. Scanning electron microscopy (SEM, Merlin, Zeiss, Germany) and stereomicroscopy (S9i, Leica, Germany) were employed to observe the surface and cross-sectional micromorphologies of the samples. An energy-dispersive spectrometer (EDS, INCA400, Oxford, Britain) was used to examine the chemical composition and elemental mapping of the coating. Using an X-ray diffractometer (XRD, X'pert Powder, PANalytical, Netherlands), the phase composition of the coating was examined. In addition, the chemical state of elements in conversion coatings was precisely characterized using X-ray photoelectron spectroscopy (XPS, Kratos Axis Ultra DLD, Kratos, United Kingdom). The XPS peak software identified each peak in the XPS spectrum, with all the peaks adjusted by the standard C 1s binding energy (284.8 eV).

2.4. Corrosion Test. The corrosion rates of the samples were determined using a 3.5 wt % NaCl solution as a test medium. In the corrosion test, the ratio of the test medium volume to the sample surface area was controlled to 50.0 mL/cm^2. A homemade device as shown in Figure 2 was employed to

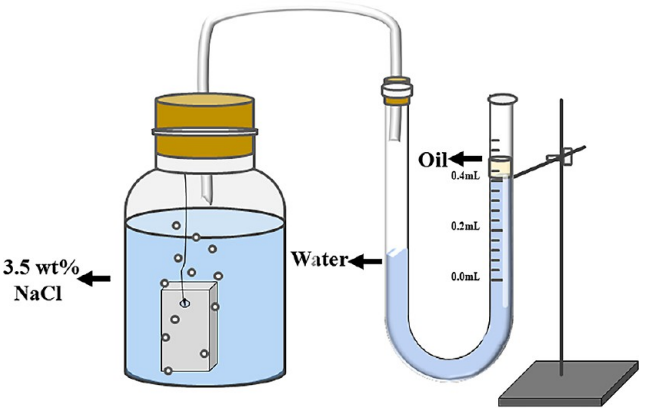

Figure 2. Home-made equipment for the HER test.

test the hydrogen evolution rate (HER) of the samples. A mass loss test was conducted to represent the corrosion rates of the samples. The corroded samples were submerged in a solution of 10.0 g/L $AgNO_3$ and 200.0 g/L CrO_3 for 5.0 min at 25.0 ± 3 °C to remove the surface corrosion products. The samples were then washed with distilled water and then weighed after being air-dried at room temperature. Equation 2 was used to determine the mass loss corrosion rate[48]

$$v_m = \frac{2.10(m_a - m_b)}{At} \quad (2)$$

where v_m is the mass loss corrosion rate in mg·cm^{-2} d^{-1}, m_a is the sample mass before the test, m_b is the sample mass after the surfaces of the corrosion products were cleaned, A is the sample surface area in cm^2, and t is the total immersion time in days.

The neutral salt spray test, according to ASTM B117-19, assessed the corrosion resistance of the coating under severe conditions. The samples were placed in a salt spray chamber at 20.0 ± 1° for 72.0 h while spraying with 5.0 wt % NaCl fog with a pH range of 6.50−7.20. The corrosion degree of the samples was evaluated using ASTM D610-08 by the Image J software.

The electrochemical workstation (Reference 600+, Gamry, America) was adopted to measure the Tafel polarization curves in 3.5 wt % NaCl solution at 25.0 ± 3 °C. The electrochemical parameters were measured in a three-electrode system with the test sample as the working electrode, a platinum plate as the counter electrode, and a saturated calomel electrode (SCE, +0.24 V vs SHE at 25.0 ± 3 °C) serving as the reference electrode. Samples should first be immersed in a 3.5 wt % NaCl solution until a constant open circuit potential (OCP) is achieved to ensure stable electrochemical impedance spectroscopy (EIS) measurements. Then, at a scan rate of 1.0 mV/s, the potentiodynamic polarization scans were performed to scan the −250.0 to +500.0 mV concerning OCP. A sine wave with an amplitude of 5.0 mV and a frequency of 10.0^{-2} to 10.0^5 Hz was used for EIS measurements. ZView software was used to analyze and fit the most recent EIS spectra.

https://doi.org/10.1021/acsomega.3c02824
ACS Omega 2023, 8, 29374−29387

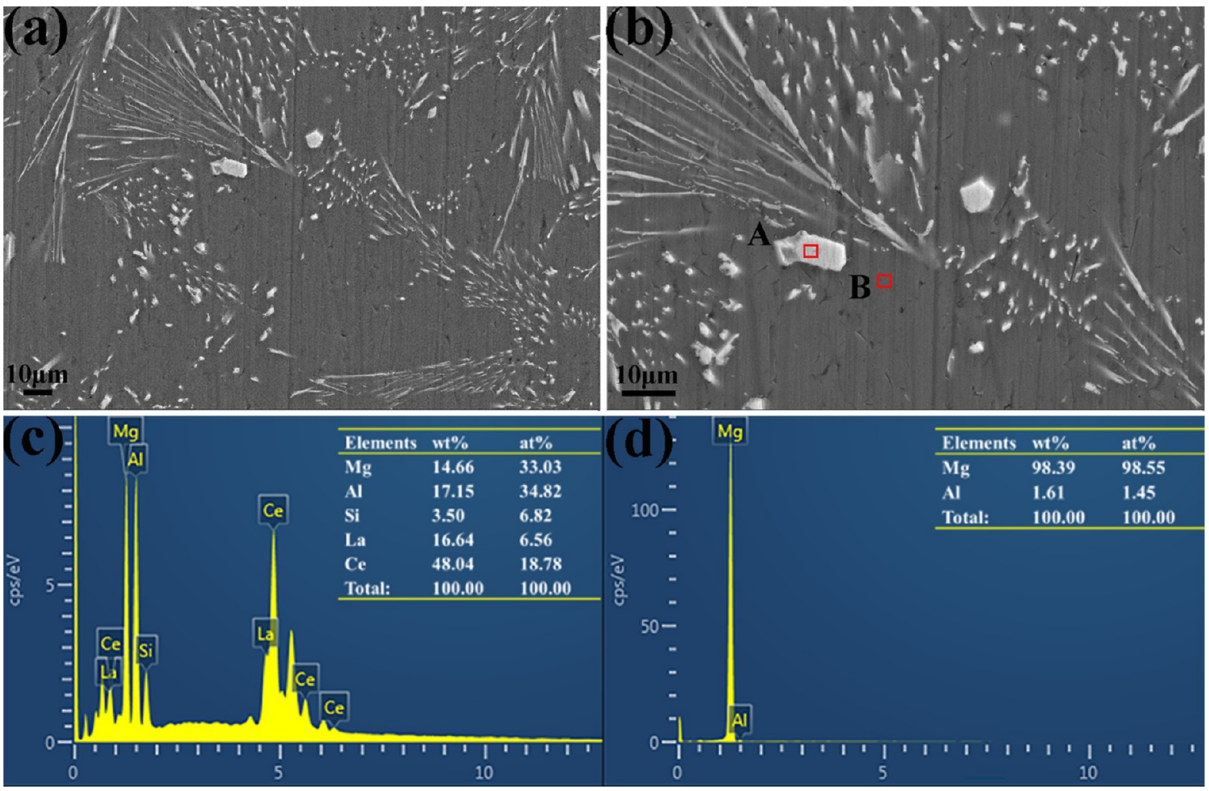

Figure 3. (a,b) SEM images of the bare sample; (c,d) EDS spectra acquired at regions A and B of the bare sample, respectively.

2.5. Adhesion Test. A tape test was carried out on the coated samples to qualitatively assess the adhesion strength between the Mg-Al-RE substrate and the composite coatings. A cross-hatch adhesion test was conducted according to the ASTM D3359-17 standard. After the test, the scratches were then compared to the standard to determine the quality of the adhesion strength.[49]

3. RESULTS AND DISCUSSION

3.1. Surface Characterization. The SEM images of the samples are displayed in Figures 3−5. Only the uncoated sample showed a few mechanical scratches after polishing. In contrast, the SEM images of the coated samples showed no evidence of previous mechanical scratches but rather a clear coating, confirming the successful preparation of the MPCC and MPCC-Si samples.

As shown in Figure 3b, the β-phase was visible. The results of the EDS analysis are depicted in Figure 3c and correspond to region A in Figure 3b, in which the β-phase of the alloy was primarily made up of Mg, La, Ce, Al, and Si. The EDS analysis of region B (Figure 3d) indicated that the α-phase of the alloy comprised Mg and Al.

The SEM of the MPCC sample is shown in Figure 4, displaying an outer layer of an embedded fragmentation film and an inner layer with localized microcracks. The region of mud cracks was covered with tiny turtle cracks. The cross-sectional SEM of the MPCC sample is shown in Figure 4f, and the thickness of the outer layer of the coating is about 3.737 ± 0.5 μm and that of the inner layer is about 0.199 ± 0.05 μm. It can be seen that the coating of the sample has larger cracks and is looser; such a structure can be easily penetrated by corrosive media, which will lead to serious corrosion of the Mg alloy. However, the MPCC-Si samples (Figure 5a−c) exhibited numerous globular converted products on the embedded fragmentation film. The converted products filled mud-like cracks and cross-linked with the fragmentation film (Figure 5b). Additionally, the cross-sectional SEM of the MPCC-Si sample is shown in Figure 5d, which revealed that the coating consisted of a dense layer of 0.355 ± 0.1 μm at the bottom and a loose layer of 6.636 ± 0.3 μm at the outside. In general, conversion coatings with microcrystalline structures exhibit better corrosion resistance, while those with coarse grains have poorer corrosion resistance. Corrosive media will more easily pass through the coating and contact with the substrate, resulting in corrosion. However, the denser conversion coating of the MPCC-Si sample and the almost crack-free base layer give it better corrosion resistance, blocking the aggression of corrosive media.

The EDS results for regions A, B, and C depicted in Figure 4c are shown in Figure 4d−f, respectively. The element P was discovered in region B, showing that the mud-crack area was also covered with a thin phosphate coating. Furthermore, the irregular region C contained La, Ce, and P elements, showing that this may be the β phase of the alloy covered with a very thin phosphate coating. The MPCC-Si coating element mapping images are displayed in Figure 6b−f. Si was scanned to indicate that APTES hydrolysate was contributing to the formation of the coating. Si elements were more dispersed in the globular-converted product region than in the mud cracks, as seen in Figure 6e. The EDS analysis results of regions A, B, and C in Figure 6a are shown in Figure 6g−i. Only in region A, which contains spherical particles, was the Si element found. Due to the addition of APTES, which covered the surface of the β-phase with the converted products, no obvious stripe or raised β-phase was present on the surface of MPCC-Si samples.

XRD was frequently used to analyze the coating components. The resulting XRD patterns of the samples (Figure 7), reveal

https://doi.org/10.1021/acsomega.3c02824
ACS Omega 2023, 8, 29374−29387

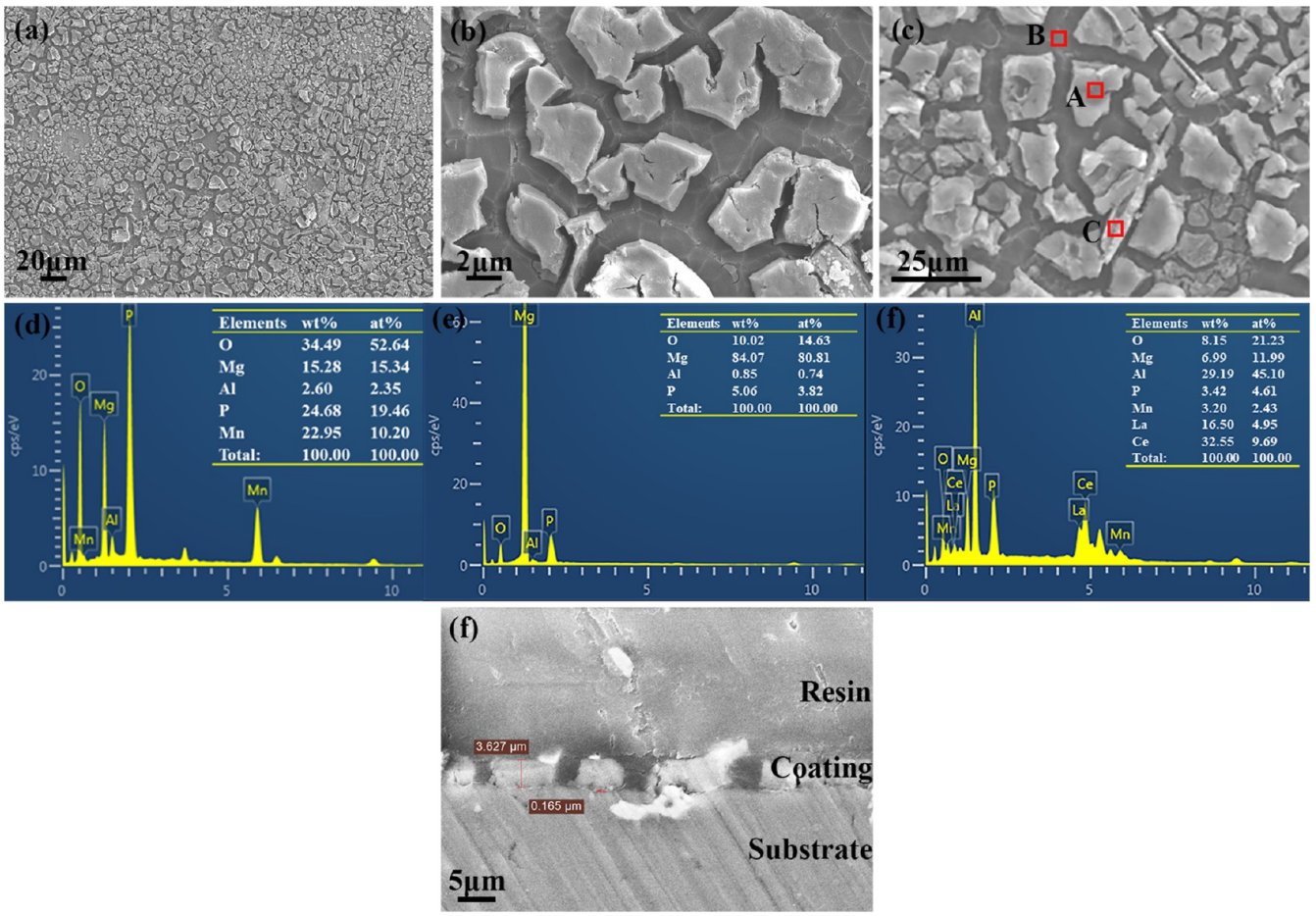

Figure 4. (a–c) SEM images of the MPCC sample; (d–f) EDS spectra acquired at regions A, B, and C of the MPCC sample, respectively; (f) cross-sectional morphologies of the MPCC-Si sample.

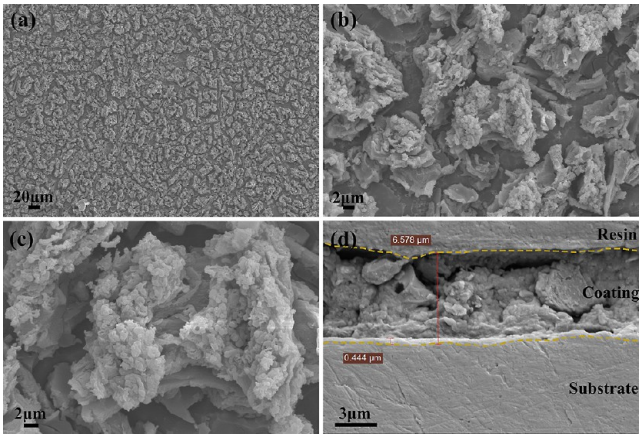

Figure 5. (a–c) Surface microstructure and (d) cross-sectional morphologies of the MPCC-Si sample.

that the MPCC-Si samples primarily contained $Mg_3(PO)_4$, $MnHPO_4$, and $Mn_3(PO_4)_2$ phases. The Si-containing inorganic phases were not detected in the test, possibly because the Si-containing compounds covered by the surface were organic. In addition, the peak intensities of the Mg-Al-RE alloy in the XRD spectrum of the MPCC coating were greater than those of the MPCC-Si coating. It may indicate that the MPCC-Si coating was denser than the MPCC coating and had fewer cracks; consequently, there was less exposure of the Mg-Al-RE alloy beneath the MPCC-Si coating. In addition, the XRD peak of the β-phase of the Mg-Al-RE alloy was weak in the spectra of the MPCC-Si coatings, indicating that the MPCC-Si coating can be formed on the β-phase.

The XPS survey spectrum of the MPCC-Si samples (Figure 8a) revealed the presence of Mn, O, P, Si, Mg, N, and C in the coating. The C 1s peak was curve-fitted to three components at 284.8 eV (C−C/C−H), 286.8 eV (C−O), and 288.6 eV (C−Si)[50,51] as shown in Figure 8b, which correspond to functional groups attributed to APTES. These findings suggested that hydrolyzed APTES played a part in the formation of the coating, which was supported by the discovery of a strong Si peak. Previous studies[52−55] indicated that the Si 2p spectrum contains four distinct types of Si bonds located at approximately 101.8, 102.2, 103.2, and 104.4 eV (Figure 8c), which were assigned to the Si-O-Mn, Si-O-Mg, Si-O-Si, and Si-C groups, respectively. Additionally, after fitting the peak of O 1s depicted in Figure 8d, four components were discovered at 531.6 eV (P−O), 531.8 eV (C−O), 532.7 eV (Si−O), and 533.8 eV (Mg-O-Si/Mn-O-Si).[53−55] Notably, the peak of the oxygen of metal oxide, which generally appears at ∼530 eV, was not detected, indicating the presence of metal oxides in the coating. The P 2p peak was curve-fitted to two components at 133.5 and 135.1 eV, as shown in Figure 8e, corresponding to HPO_4^{2-} and PO_4^{3-}, respectively.[36,56] The primary and secondary peaks correspond to the Mn $2p_{3/2}$ (642.1 eV) and Mn $2p_{1/2}$ (652.9 eV)[36] spin−orbit energy levels seen in the spectrum (Figure 8f). Meanwhile, the

https://doi.org/10.1021/acsomega.3c02824
ACS Omega 2023, 8, 29374−29387

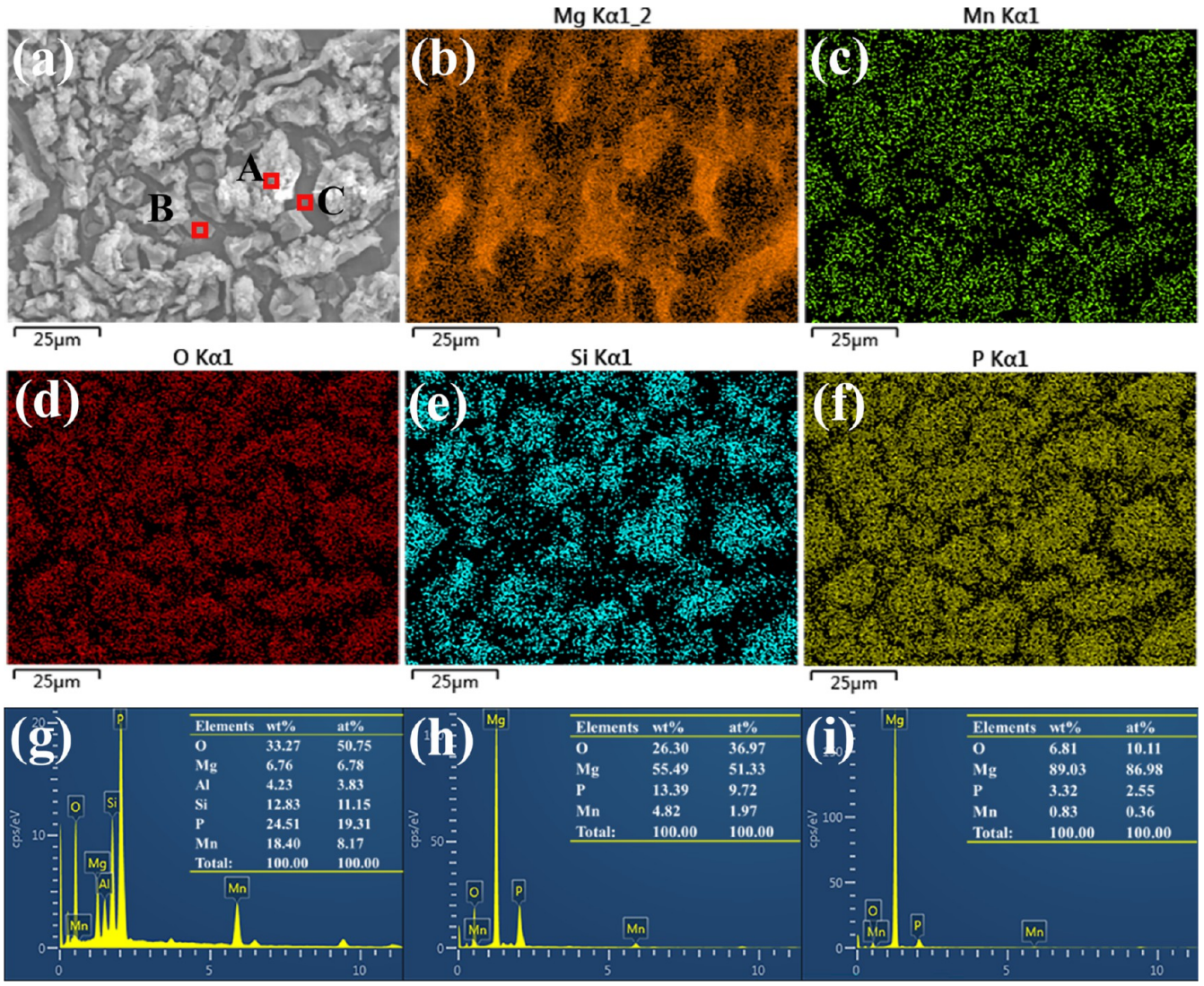

Figure 6. (a–f) Mapping images of the EDS area of the MPCC-Si sample; (g–i) EDS spectra acquired at regions A, B, and C of the MPCC-Si sample, respectively.

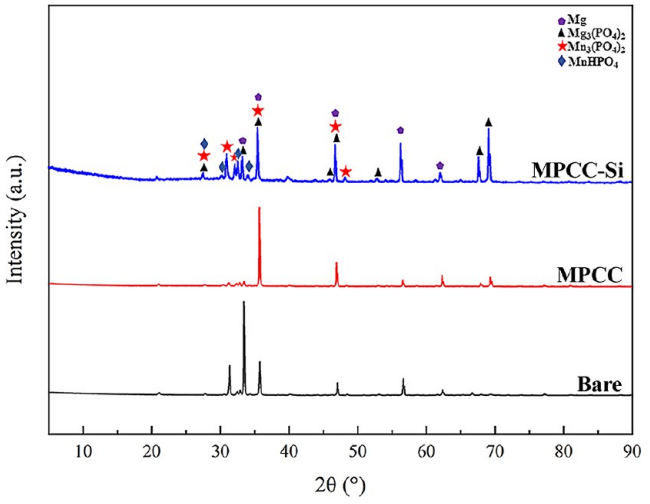

Figure 7. XRD patterns of the bare, MPCC, and MPCC-Si samples.

secondary peaks at higher binding energies represented the satellite peaks (645.6 and 658.4 eV).

3.2. Properties of Conversion Coating. *3.2.1. Hydrogen Evolution Test and Mass Loss Test.* The photograph of various samples before and after the hydrogen evolution test is shown in Figure 9. Due to the accelerated corrosion of microgalvanic for the substrate phase by the contiguous β-phase particle, significant partial corrosion can be seen on the Mg-Al-RE alloy surface after 4 h of immersion. The sample showed numerous filiform and white pitting corrosion products after 96 h of immersion. The sample color changed significantly, indicating that the alloy had been severely corroded. The MPCC sample displayed apparent pitting corrosion after 12 h of immersion, and the color changed after 96 h of immersion. However, the pitting corrosion was less severe than that observed on the uncoated sample. After 24 h of immersion, the MPCC-Si sample appeared to have white pitting corrosion products, and the sample had a little variation in color. The amount of pitting on the MPCC-Si sample was also the lowest, indicating that the corrosion rate of the sample was significantly reduced after this conversion treatment with the APTES-phosphate solution. The average mass loss rate of the samples is shown in Figure 10a, with the bare sample exhibiting the highest mass loss rate, followed by the MPCC sample, and the MPCC-Si

https://doi.org/10.1021/acsomega.3c02824
ACS Omega 2023, 8, 29374−29387

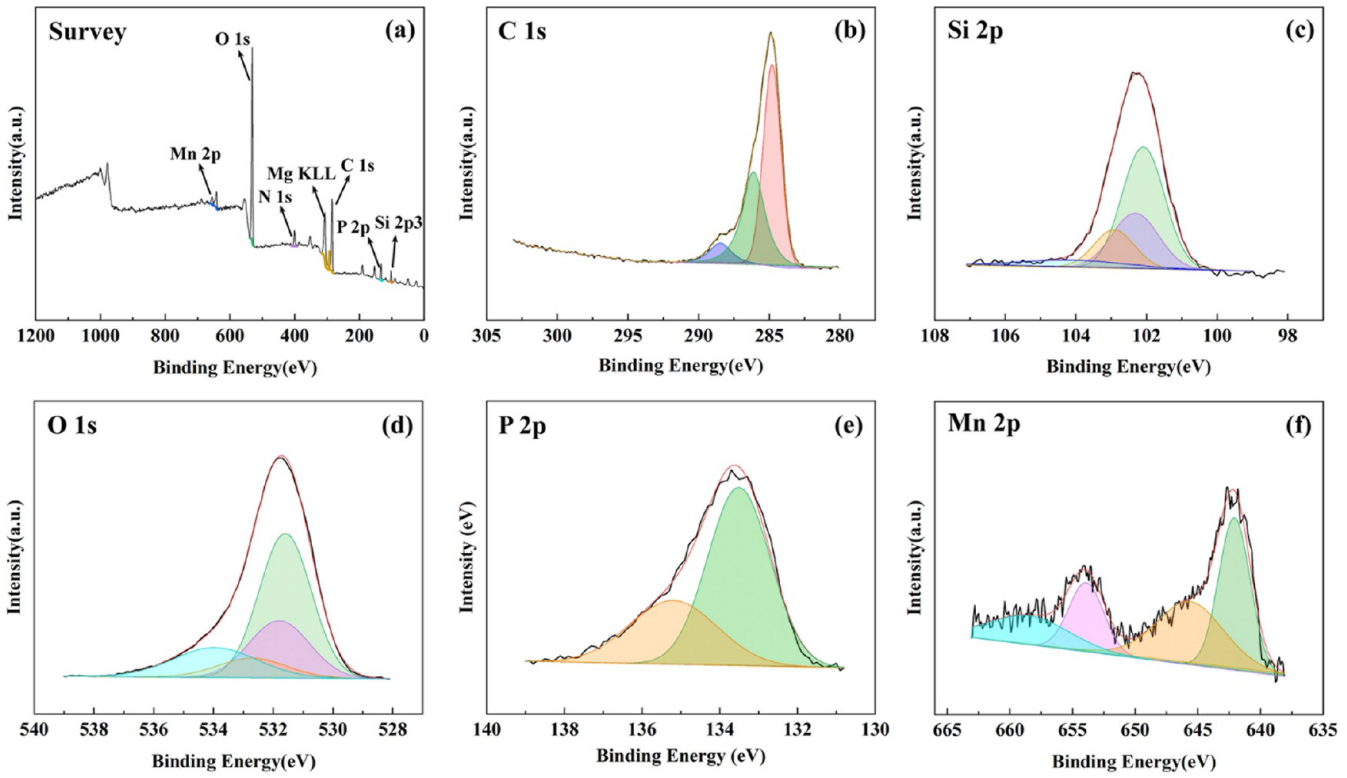

Figure 8. XPS spectrum of the MPCC-Si sample, (a) survey, (b) C 1s, (c) Si 2p, (d) O 1s, (e) P 2p, and (f) Mn 2p.

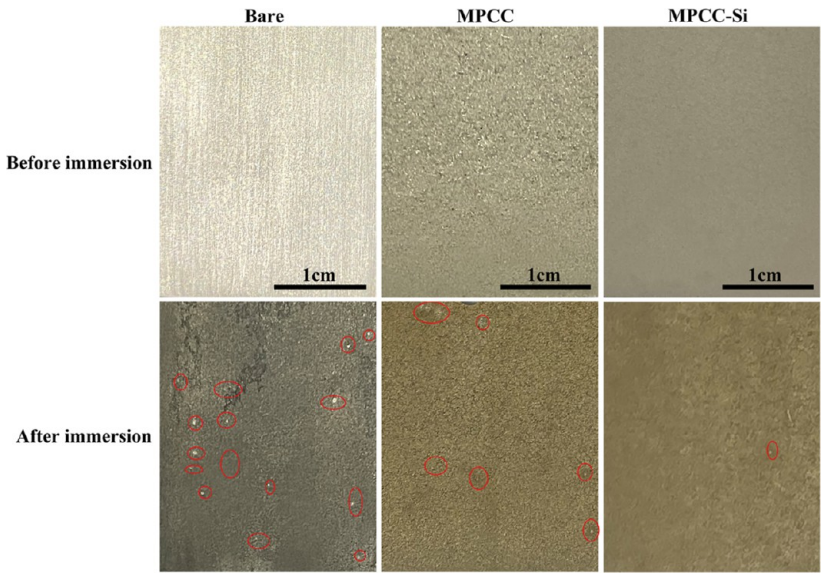

Figure 9. Morphology of samples before and after immersion for 96 h.

sample exhibiting the lowest mass loss rate during the total 96 h test time. The results of the HER test (Figure 10b) indicated that the MPCC-Si sample possessed the lowest HER and the best corrosion resistance, which is consistent with the level of corrosion observed on the sample surface.

3.2.2. Salt Spray Test. The morphology of the samples before and after 72 h SST is shown in Figure 11. The bare sample was severely corroded, resulting in the formation of several substantial black corrosion areas. After 12 h of SST, the bare sample had a corroded area of about 40%. However, after 12 h of SST, the MPCC sample only showed a few pitting rusts. Surprisingly, only a pitting spot appeared on the MPCC-Si sample after 36 h of SST. Table 2 displays the corrosion surface area percentages and rust grade of various samples evaluated after 72 h of SST using ImageJ software following ASTM D610-08. Notably, the corrosion surface area of the MPCC-Si sample after 72 h of SST was only about 0.28% (rust grade 7), demonstrating the highest corrosion resistance. These results suggest that the coating obtained by the APTES-phosphate solution could better inhibit the aggressive media when exposed to a harsh environment. These results were consistent with the HER and mass loss test outcomes.

3.2.3. Electrochemical Analysis. The electrochemical test results of the samples in the 3.5 wt % NaCl solution are displayed

https://doi.org/10.1021/acsomega.3c02824
ACS Omega 2023, 8, 29374−29387

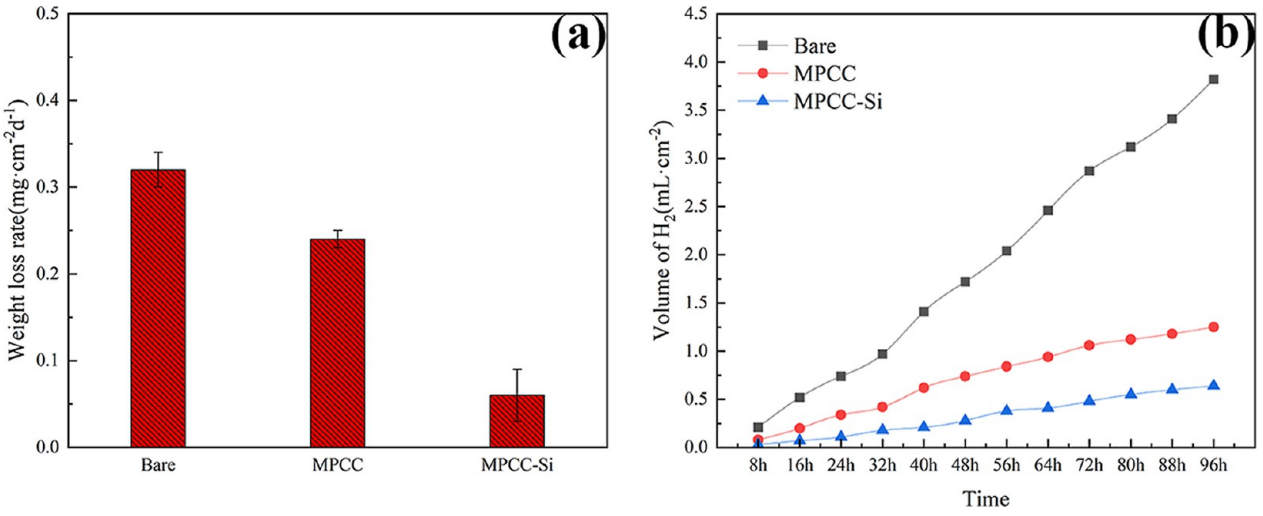

Figure 10. (a) Average mass loss rate of the samples; (b) H_2 volume of the samples.

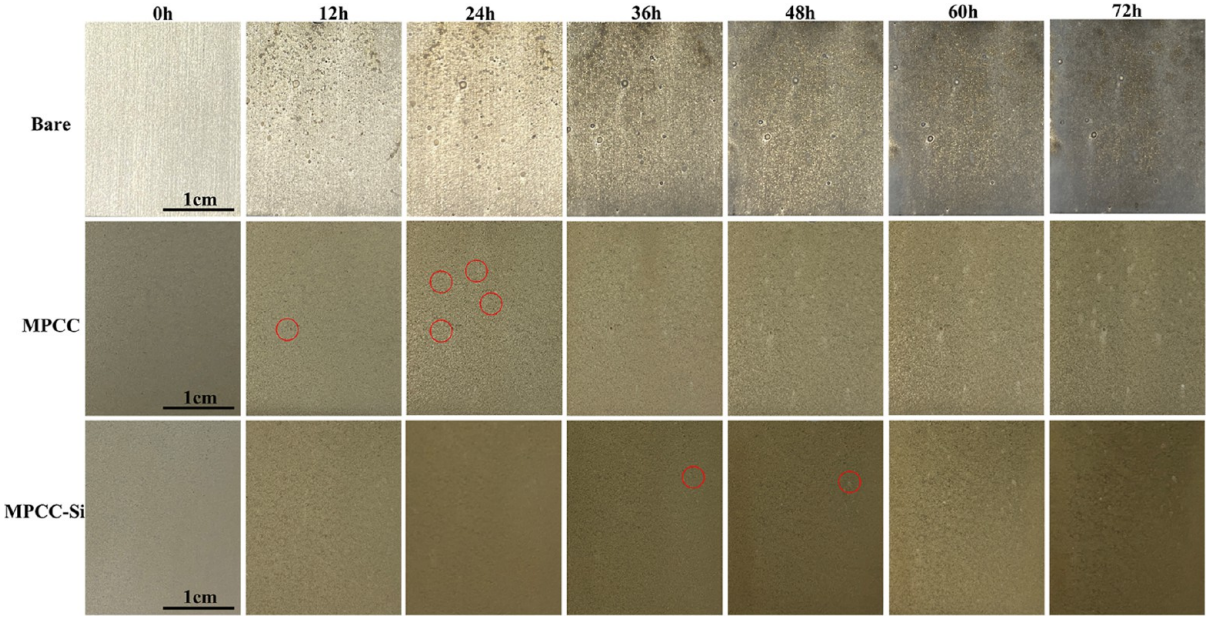

Figure 11. Visual images of the bare and coated samples after 72 h of SST.

Table 2. Corrosion Area Fraction and Rust Grade of Different Samples after 72 h of SST

samples	test time (h)	corrosion area fraction (%)	rust grade
bare	72	96.71	0
MPCC	72	2.13	5
MPCC-Si	72	0.28	7

in Figure 12. The Tafel extrapolation method was used to fit corrosion current densities (i_{corr}) and potentials (E_{corr}). After conversion treatment, the i_{corr} values of the samples for anodic and cathodic branches were inhibited, while the E_{corr} values increased.[21] The shift in E_{corr} toward the anodic direction suggested that the conversion coating functions as a physical barrier to prevent electrolyte penetration.[57] Compared to the bare sample, the i_{corr} was reduced by less than 1 order of magnitude for the MPCC sample and by 2 for the MPCC-Si sample. The difference in i_{corr} values of the two samples may be due to the higher densities of the MPCC-Si sample and the smaller microcracks on the surface, which effectively inhibit the corrosion of the substrate. This result was consistent with the results of the hydrogen evolution test and suggests that MPCC-Si possesses better corrosion protection capabilities. The summary of the E_{corr} and i_{corr} values of samples is provided in Table 3.

The relationship between the i_{corr} and the corrosion rate P_i can be interpreted by eq 3.[58] The P_i values of the samples calculated from the measured i_{corr} values is presented in Table 4. The results indicated that the MPCC-Si sample had the lowest P_i value (0.015 mm/y), compared to 0.238 mm/y for MPCC and 1.780 mm/y for the bare sample. The protection efficiency (η, %) is determined by eq 4,[37] where i^0_{corr} and i_{corr} are the corrosion current densities of the bare and different covered samples, respectively. According to Table 3, the MPCC-Si sample had the highest corrosion resistance and the lowest P_i value.

$$P_i = 22.85 i_{corr} \quad (3)$$

https://doi.org/10.1021/acsomega.3c02824
ACS Omega 2023, 8, 29374−29387

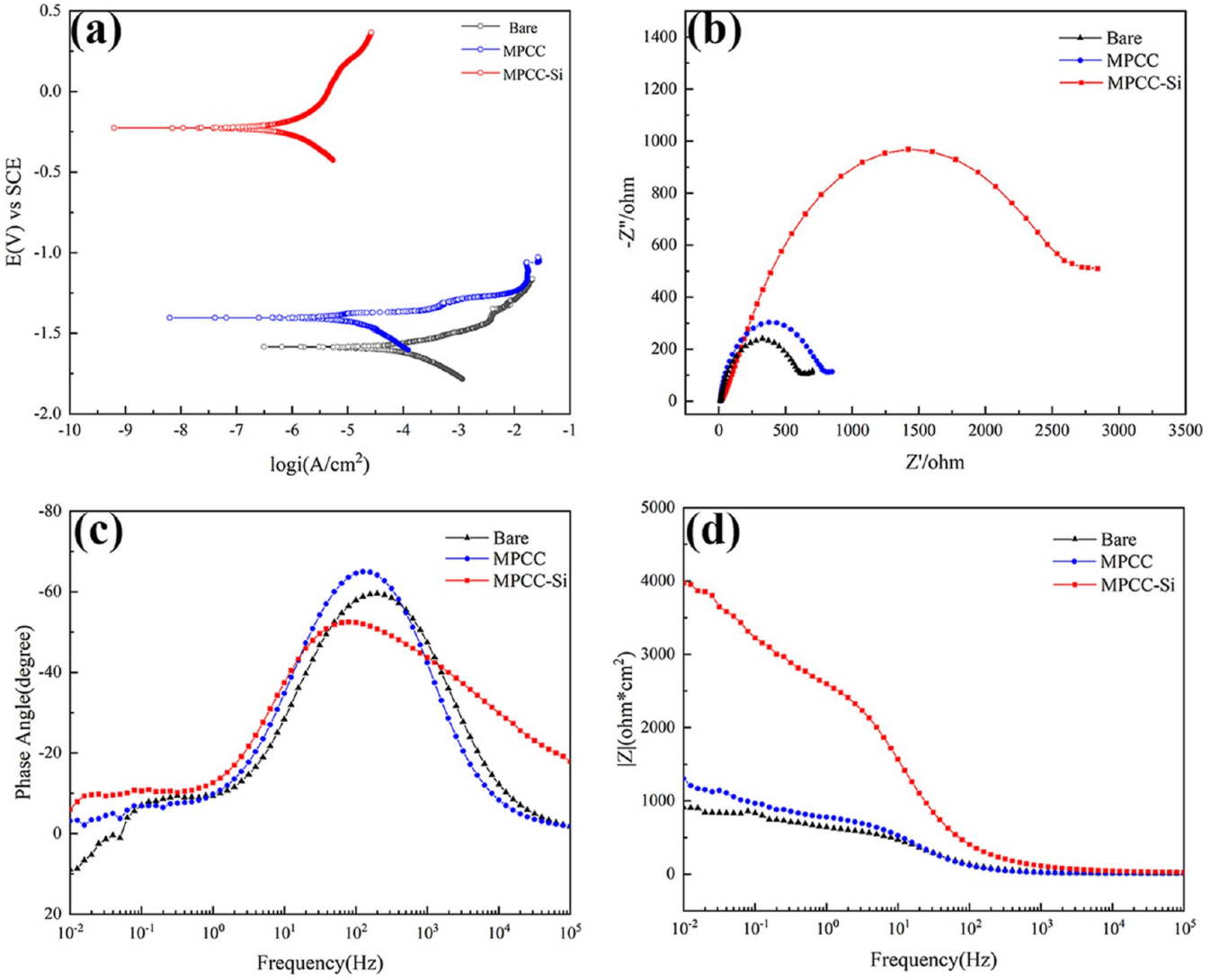

Figure 12. (a) Potentiodynamic polarization curves, (b) Nyquist plots, (c) Bode impedance plots, and (d) Bode phase angle plots.

Table 3. Fitting Results of the Polarization Curves and η

sample	E_{corr} (V)	i_{corr} (A/cm^2)	P_i (mm/y)	H (%)
bare	−1.584	7.790×10^{-5}	1.780	
MPCC	−1.377	1.043×10^{-5}	0.238	86.611
MPCC-Si	−0.224	6.678×10^{-7}	0.015	99.143

$$\eta = \frac{i_{corr}^{0} - i_{corr}}{i_{corr}} \times 100\% \quad (4)$$

The Nyquist plots of the samples obtained through cathodic electrochemical treatment are shown in Figure 12b. The plot revealed a single capacitive loop for all the samples (Figure 12b). In general, the larger the radius of the capacitive loop of the sample, the better the corrosion resistance.[47] The high-frequency region primarily reflected the barrier properties of the coating. In contrast, the low-frequency region was primarily associated with the diffusion-type corrosion reaction at the metal coating interface.[59] The addition of silane increased the phase angle of the MPCC-Si sample at high frequency, which was attributed to an increase in coating thickness and a decrease in defects.[52] In addition, the Bode plots in Figure 12c showed that MPCC-Si exhibits the highest impedance |Z| at 0.01 Hz, and no apparent resistive plateau was observed, indicating excellent corrosion resistance.[53]

Using Zview software, an equivalent electrical circuit model (Figure 13) was proposed to fit the EIS test data. In addition, the incomplete capacitive loops in the Nyquist plots may also help explain the nonuniformity caused by the coating (Figure 12b). The constant phase element (CPE), which replaced capacitance, can be used to calculate Q as follows[60]

Table 4. Electrochemical Parameters Gained from the Fitting Results of EIS Data

sample	R_s (Ω cm^2)	R_c (Ω cm^2)	CPE_c (Ω^{-1} S^n cm^{-2})	n_1	R_{ct} (Ω cm^2)	CPE_{dl} (Ω^{-1} S^n cm^{-2})	n_2	R_P (Ω cm^2)	PE %
Bare	14.30	661.00	9.70×10^{-4}					661.00	
MPCC	13.42	733.80	2.86×10^{-1}	0.88	457.50	2.95×10^{-3}	0.80	1191.30	44.51
MPCC-Si	23.76	3252.00	3.37×10^{-5}	0.65	977.40	4.95×10^{-4}	0.99	4299.40	84.62

https://doi.org/10.1021/acsomega.3c02824
ACS Omega 2023, 8, 29374−29387

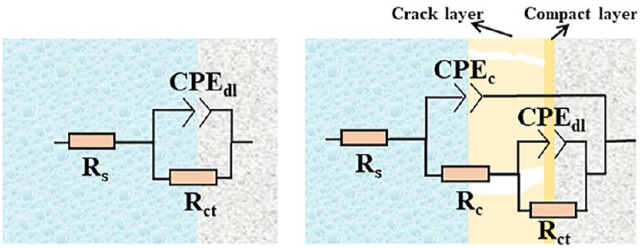

Figure 13. Electrical equivalent circuit used to fit impedance data.

$$Z_{CPE} = \frac{1}{Q(j\omega)^n} \quad (5)$$

where $\omega = 2f$, in which f is the frequency, n is a CPE index involving the roughness of the coating, and CPE_{dl} and CPE_c stand for the double-layer and coating capacitances, respectively. In the equivalent electric circuit model, R_c, R_s, and R_{ct} represent the coating resistance, the solution resistance, and the charge transfer resistance, respectively. The polarization resistance R_p is the sum of R_{ct} and R_c and was applied to calculate the protection efficiency (PE, eq 6) of the coatings[61]

$$PE\ \% = \frac{R_P^{EC} - R_P^0}{R_P} \quad (6)$$

where R_P^{EC} and R_P^0 are the polarization resistances in the coated and uncoated samples, respectively. The deduced R_P and PE values of the samples are summarized in Table 4. The MPCC-Si sample exhibited the highest R_p (4299.40 $\Omega \cdot cm^2$), while the PE was 84.62%, revealing a better corrosion resistance for the sample.

3.2.4. Adhesion Test. Since the adhesion of the coating has a significant impact on the anti-corrosion ability of the coated sample, a tape test was performed to assess the adhesive quality of the samples. The images of the sample before and after the test are shown in Figure 14. The tape test revealed a little peeling or separation of the coatings, and the coating/substrate adhesion level was classified as 5B based on the ASTM D3359-17 standard. This indicates that the organic/inorganic composite coating composed of silane hydrolysate is well bonded to the substrate and can perform well in corrosion protection.

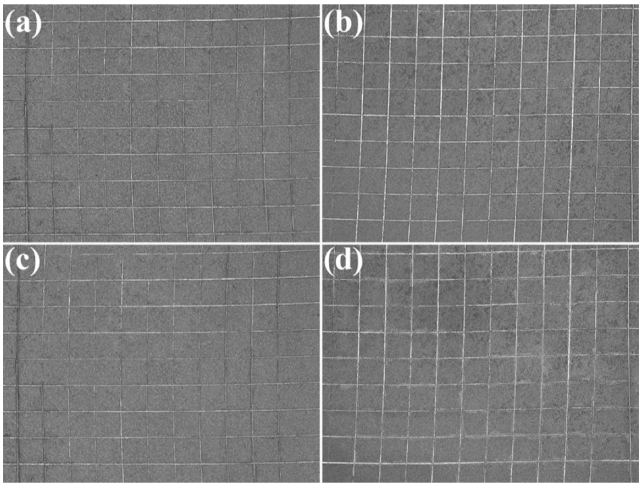

Figure 14. Digital image of MPCC and MPCC-Si samples by the tape test, (a,b) MPCC and MPCC-Si samples before the test, respectively. (c) and (d) MPCC and MPCC-Si samples after the test, respectively.

3.3. Mechanism of MPCC-Si Coating Formation. Based on XPS, SEM, and EDS analyses, it was determined that the formation of the MPCC-Si coating on the Mg-Al-RE alloy occurred in three stages, as depicted in Figure 15. After immersion in the phosphate conversion solution, the formation of the microgalvanic couples on the substrate surface was attributed to different phase potentials of α and β. Therefore, the first stage consisted of the dissolution of magnesium as an anode in the acidic conversion solution (eq 7) and the release of hydrogen from the β phase (eqs 8 and 9)[36]

$$Mg \rightarrow Mg^{2+} + 2e^- \quad (7)$$

$$H_2O \rightarrow OH^- + H^+ \quad (8)$$

$$H^+ + 2e^- \rightarrow H_2\uparrow \quad (9)$$

The second stage should be phosphate deposition, as shown in Figure 15b. Since the K_{sp} value of Mg phosphates was 10^{-20} or lower,[37] the deposition of $Mg_3(PO_4)_2$ (eq 10) began when the Mg alloy was dissolved. Then, an interlaminar block composed primarily of magnesium phosphate and manganese phosphate (eqs 11 and 12) began to form. The complex formed by PO_4^{3-} or HPO_4^{2-} and APTES hydrolysates likewise contributed to this process.

$$3Mg^{2+} + 2PO_4^{3-} \rightarrow Mg_3(PO_4)_2\downarrow \quad (10)$$

$$H_2PO_4^- \rightarrow HPO_4^{2-} + H^+ \quad (11)$$

$$4Mn^{2+} + 3HPO_4^{2-} \rightarrow MnHPO_4\downarrow + Mn_3(PO_4)_2\downarrow + 5H^+ \quad (12)$$

As depicted in Figure 15c, the final stage should be the self-condensation reaction of APTES hydrolysates. Most Si-OH groups produced by the hydrolysis of APTES bind to one another to form a stable Si-O-Si network (eqs 13 and 14), which provides the required chemical stability and anti-corrosion properties. As depicted in Figure 15c, this results in the formation of clusters of silicon-containing compounds on the block area.

$$Si\text{-}OH + Si\text{-}OH \rightarrow Si\text{-}O\text{-}Si + H_2O \quad (13)$$

$$Si\text{-}O\text{-}Si\text{-}OH + Si\text{-}OH \rightarrow Si\text{-}O\text{-}Si\text{-}O\text{-}Si\text{-}O + H_2O \quad (14)$$

3.4. Corrosion Mechanism. As can be seen in Figure 9, a lot of black filiform corrosion, as well as white pitting appeared on the bare sample after 96 h of immersion in 3.5 wt % NaCl solution. This suggests that filiform corrosion can lead to relatively resistive oxides on the Mg-Al-RE alloy, and these oxides can be cracked by hydrogen evolution during the corrosion of the substrate. The Cl^- ions in the corrosion medium can accelerate the corrosion of the alloy, and this mechanism can be illustrated by the following equation[62,63]

$$Mg \rightarrow Mg^{2+} + 2e^- \quad (15)$$

$$H_2O - 2e^- \rightarrow 2OH^- + H_2\uparrow \quad (16)$$

$$Mg^{2+} + 2OH^- \rightarrow Mg(OH)_2 \quad (17)$$

$$2Cl^- + Mg(OH)_2 \rightarrow MgCl_2 + 2OH^- \quad (18)$$

For the MPCC-Si sample, no filiform corrosion is observed, and only a few pitting corrosions are confirmed, indicating that its corrosion resistance performance is excellent. A possible

https://doi.org/10.1021/acsomega.3c02824
ACS Omega 2023, 8, 29374−29387

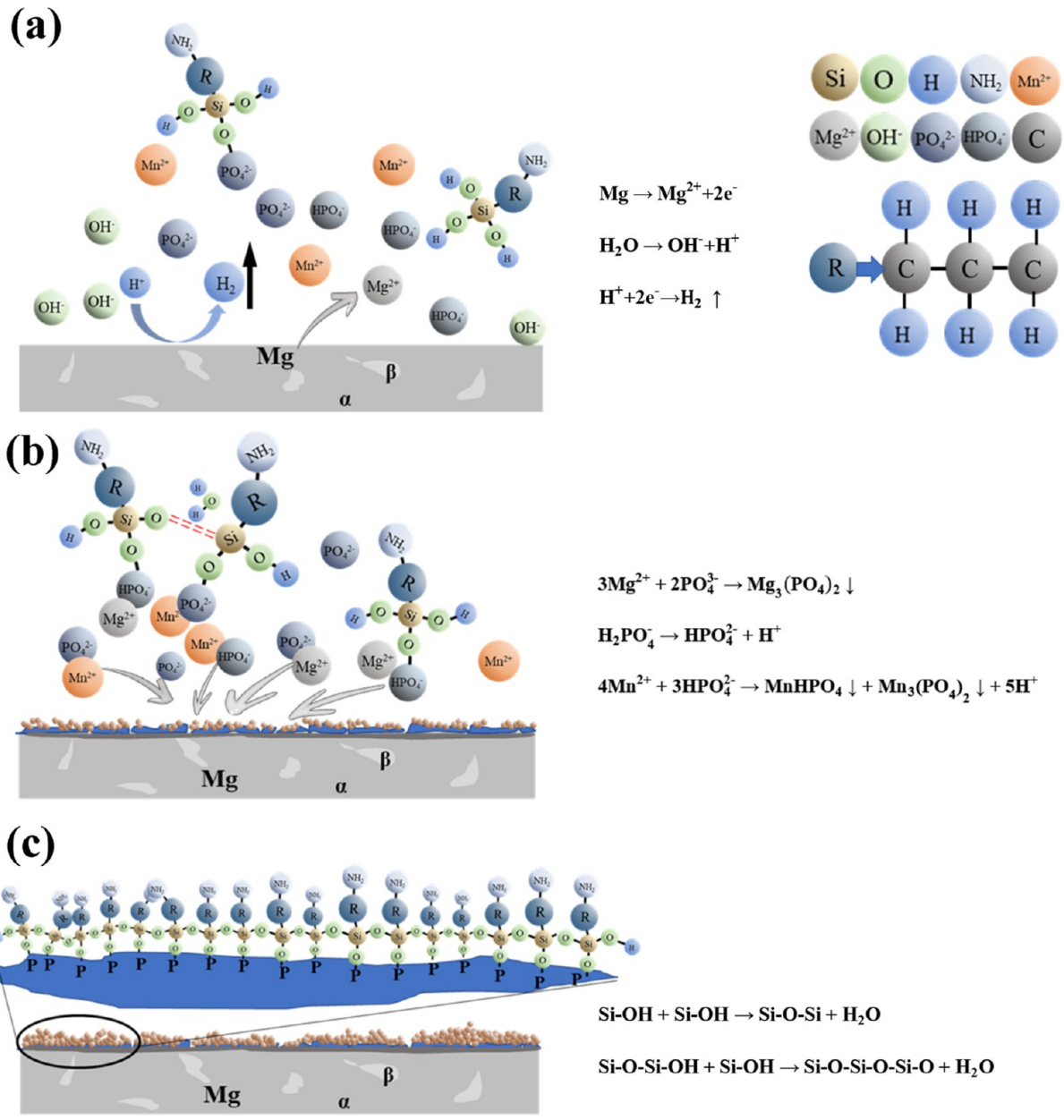

Figure 15. Schematic of the initial formation process of the MPCC-Si coating on the Mg-Al-RE alloy: (a) first stage, (b) second stage, and (c) third stage.

corrosion mechanism of the MPCC-Si sample is presented to further understand the corrosion behavior of the sample, which is shown in Figure 16. In the first stage, the corrosion medium permeates into the interface between the substrate and coating through the pores and cracks in the conversion coating and makes the Mg-Al-RE alloy dissolve. Then, the local pH value increases, causing partly alkaline dissolution and breakage of the coating. However, the coating is a non-conducting layer that is well bonded to the alloy surface, and therefore the corrosion medium is unable to diffuse sideways. Finally, the coating damaged area forms a small anode-large cathode autocatalytic system on the longitudinal and results in pitting corrosion. The coating acts as a physical barrier against the penetration of corrosive media,[57] thus providing protection to the Mg-Al-RE alloy. However, defects in the coating such as micro cracks will weaken its corrosion resistance and protection durability.[47] Moreover, the thickness and density of the coating affect its corrosion resistance. Both surface and cross-sectional SEM images show that the MPCC-Si sample exhibits a denser structure , thicker coating, and fewer surface cracks than the MPCC sample. Therefore, the MPCC-Si sample can play a better role as a physical barrier, which can protect the Mg alloy better.

4. CONCLUSIONS

1. In this way, a highly corrosion-resistant organic/inorganic double-layer composite conversion coating can be prepared in one step. In addition, it can form a coating in a very short time, which greatly improves the production efficiency.
2. Higher surface coverage and a denser conversion coating result from APTES' involvement in the coating formation process.

https://doi.org/10.1021/acsomega.3c02824
ACS Omega 2023, 8, 29374−29387

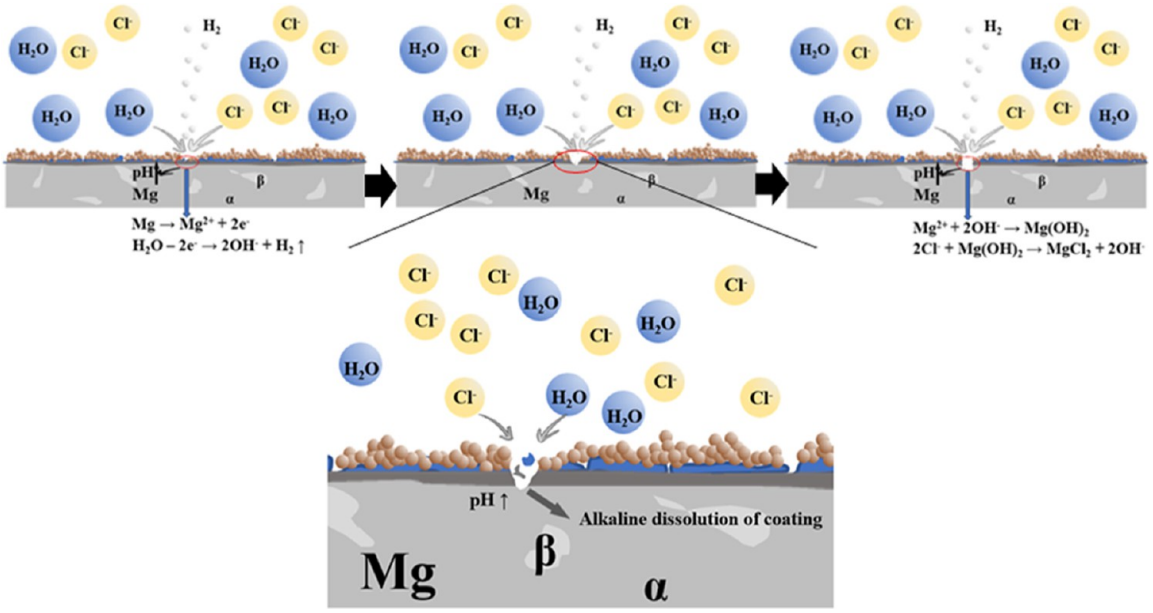

Figure 16. Schematic diagrams of the corrosion mechanism for the MPCC-Si sample.

3. The samples prepared with the phosphate-APTES solution exhibited the best corrosion resistance. Compared to the bare Mg alloy, the i_{corr} value of the MPCC-Si sample with APTES reduced by 2 orders of magnitude, while the E_{corr} value increased by 1.360 V. The salt spray resistance time was up to 36 h, and the rust grade could still reach 7 after 72 h of SST.

AUTHOR INFORMATION

Corresponding Author

Yongjun Zhang − *School of Mechanical and Automotive Engineering, South China University of Technology, Guangzhou 510640, P. R. China;* orcid.org/0000-0002-9704-9577; Email: zhangyj@scut.edu.cn

Author

Haoyu Wang − *School of Mechanical and Automotive Engineering, South China University of Technology, Guangzhou 510640, P. R. China;* orcid.org/0009-0009-9669-9744

Complete contact information is available at: https://pubs.acs.org/10.1021/acsomega.3c02824

Author Contributions

H.W.: Conceptualization, methodology, writing-original draft, formal analysis, and investigation. Y.Z.: Conceptualization, writing-review & editing, resources, and investigation.

Notes

The authors declare no competing financial interest.
No data was used for the research described in the article.

ACKNOWLEDGMENTS

Most of the work in this paper was supported by the Natural Science Foundation of Guangdong Province, P. R. China (no. 2023A1515011202).

REFERENCES

(1) Zeng, Z.; Nie, J.-F.; Xu, S.-W.; Davies, C. H. J.; Birbilis, N. Superformable pure magnesium at room temperature. *Nat. Commun.* **2017**, *8*, 972.

(2) Mordike, B. L.; Ebert, T. Magnesium: Properties-applications-potential. *Mater. Sci. Eng., A* **2001**, *302*, 37−45.

(3) Jian, S. Y.; Yang, C. Y.; Chang, J. K. Robust corrosion resistance and self-healing characteristics of a novel Ce/Mn conversion coatings on EV31 magnesium alloys. *Appl. Surf. Sci.* **2020**, *510*, 145385.

(4) Ebrahimi, M.; Wang, Q. D.; Attarilar, S. A comprehensive review of magnesium-based alloys and composites processed by cyclic extrusion compression and the related techniques. *Prog. Mater. Sci.* **2023**, *131*, 101016.

(5) Venugopal, S.; Karikalan, L.; Kumar, R. Experimental investigations on the effect of reinforcement coating on magnesium composites for automotive brake pad. *Adv. Mater. Sci. Eng.* **2022**, *2022*, 7604681.

(6) Zhu, S. M.; Easton, M. A.; Abbott, T. B.; Gibson, M. A.; Nie, J. F. The influence of individual rare earth elements (La, Ce, or Nd) on creep resistance of die-cast magnesium alloy AE44. *Adv. Eng. Mater.* **2016**, *18*, 932−937.

(7) Willbold, E.; Gu, X. N.; Albert, D.; Kalla, K.; Bobe, K.; Brauneis, M.; Janning, C.; Nellesen, J.; Czayka, W.; Tillmann, W.; Zheng, Y. F.; Witte, F. Effect of the addition of low rare earth elements (lanthanum, neodymium, cerium) on the biodegradation and biocompatibility of magnesium. *Acta Biomater.* **2015**, *11*, 554−562.

(8) Liang, M. J.; Liu, H.; Wu, C.; Li, Y. D.; Guo, Z. H.; Murugadoss, V. Effects of rare earth neodymium (Nd) and heat treatment on anti-corrosion behaviors of the AZ80 magnesium alloy. *Adv. Compos. Hybrid Mater.* **2022**, *5*, 1460−1476.

(9) Song, J. F.; Chen, J.; Xiong, X. M.; Peng, X. D.; Chen, D. L.; Pan, F. S. Research advances of magnesium and magnesium alloys worldwide in 2021. *J. Magnesium Alloys* **2022**, *10*, 863−898.

(10) Xiang, T. F.; Zheng, S. L.; Zhang, M.; Sadig, H. R.; Li, C. Bioinspired slippery zinc phosphate coating for sustainable corrosion protection. *ACS Sustainable Chem. Eng.* **2018**, *6*, 10960−10968.

(11) Li, D. Y.; Cui, X. F.; Wen, X.; Feng, L. T.; Hu, Y. T.; Jin, G.; Liu, E. B.; Zheng, W. Effect of CeO_2 nanoparticles modified graphene oxide on electroless Ni-P coating for Mg-Li alloys. *Appl. Surf. Sci.* **2022**, *593*, 153381.

(12) Wen, F. L.; Zhao, J. H.; Yuan, M. W.; Wang, J. F.; Zheng, D. Z.; Zhang, J. Y.; He, K.; Shangguan, J. J.; Guo, Y. Influence of Ni interlayer on interfacial microstructure and mechanical properties of Ti-6Al-4V/

https://doi.org/10.1021/acsomega.3c02824
ACS Omega 2023, 8, 29374−29387

AZ91D bimetals fabricated by a solid-liquid compound casting process. *J. Magnesium Alloys* **2021**, *9*, 1382−1395.
(13) Hu, R. G.; Zhang, S.; Bu, J. F.; Lin, C. J.; Song, G. L. Recent progress in corrosion protection of magnesium alloys by organic coatings. *Prog. Org. Coat.* **2012**, *73*, 129−141.
(14) Liu, C. C.; Liang, J.; Zhou, J. S.; Wang, L. Q.; Li, Q. B. Effect of laser surface melting on microstructure and corrosion characteristics of AM60B magnesium alloy. *Appl. Surf. Sci.* **2015**, *343*, 133−140.
(15) Nezamdoust, S.; Seifzadeh, D.; Rajabalizadeh, Z. Application of novel sol-gel composites on magnesium alloy. *J. Magnesium Alloys* **2019**, *7*, 419−432.
(16) Qin, J.; Shi, X. T.; Li, H. Y.; Zhao, R. F.; Li, G. Q.; Zhang, S. F.; Ding, L. Y.; Cui, X. J.; Zhao, Y.; Zhang, R. F. Performance and failure process of green recycling solutions for preparing high degradation resistance coating on biomedical magnesium alloys. *Green Chem.* **2022**, *24*, 8113−8130.
(17) Morini, F.; Bestetti, M.; Franz, S.; Vicenzo, A.; Markov, A.; Yakovlev, E. Surface properties modification of magnesium alloys by low energy high current pulsed electron beam. *Surf. Coat. Technol.* **2021**, *420*, 127351.
(18) Hafeez, M. A.; Farooq, A.; Zang, A.; Saleem, A.; Deen, K. M. Phosphate chemical conversion coatings for magnesium alloys: a review. *J. Coat. Technol. Res.* **2020**, *17*, 827−849.
(19) Hu, L. F.; Meng, Q. S.; Chen, S. P.; Wang, H. Effect of Zn content on the chemical conversion treatments of AZ91D Magnesium alloy. *Appl. Surf. Sci.* **2012**, *259*, 816−823.
(20) Pommiers, S.; Frayret, J.; Castetbon, A.; Potin-Gautier, M. Alternative conversion coatings to chromate for the protection of magnesium alloys. *Corros. Sci.* **2014**, *84*, 135−146.
(21) Jian, S. Y.; Chang, K. L. Effect of cerium ion on the microstructure and properties of permanganate conversion coating on LZ91 magnesium alloy. *Appl. Surf. Sci.* **2020**, *509*, 144767.
(22) Liao, S. J.; Yu, B. X.; Zhang, X. L.; Lu, X. P.; Zhou, P.; Zhang, C. Y.; Chen, X. B.; Zhang, T.; Wang, F. H. New design principles for the bath towards chromate- and crack-free conversion coatings on magnesium alloys. *J. Magnesium Alloys* **2021**, *9*, 505−519.
(23) Salman, S. A.; Gouda, M. K. Characterization and corrosion behavior of vanadium-based conversion coating on AZ31 magnesium alloy. *Mater. Today: Proc.* **2022**, *62*, 611−614.
(24) Lee, Y. L.; Chu, Y. R.; Li, W. C.; Lin, C. S. Effect of permanganate concentration on the formation and properties of phosphate/permanganate conversion coating on AZ31 magnesium alloy. *Corros. Sci.* **2013**, *70*, 74−81.
(25) Elsentriecy, H. H.; Azumi, K.; Konno, H. Improvement in stannate chemical conversion coatings on AZ91D magnesium alloy using the potentiostatic technique. *Electrochim. Acta* **2007**, *53*, 1006−1012.
(26) Chen, J.; Song, Y. W.; Shan, D. Y.; Han, E. H. In situ growth of Mg-Al hydrotalcite conversion film on AZ31 magnesium alloy. *Corros. Sci.* **2011**, *53*, 3281−3288.
(27) Kamde, M. A.; Mahton, Y.; Ohodnicki, J.; Roy, M.; Saha, P. Effect of cerium-based conversion coating on corrosion behavior of squeeze cast Mg-4 wt% Y alloy in 0.1 M NaCl solution. *Surf. Coat. Technol.* **2021**, *421*, 127451.
(28) Gou, J. F.; Sun, M. R.; Ma, X. X.; Tang, G. Z.; Zhang, Y. K. Effects of temperature and pH value on the morphology and corrosion resistance of titanium-containing conversion coating. *Appl. Surf. Sci.* **2021**, *3*, 100060.
(29) Fockaert, L. I.; Pletincx, S.; Boelen, B.; Hauffman, T.; Terryn, H.; Mol, J. M. C. Effect of zirconium-based conversion treatments of zinc, aluminium and magnesium on the chemisorption of ester-functionalized molecules. *Appl. Surf. Sci.* **2020**, *508*, 145199.
(30) Liu, L.; Yang, Q. Y.; Huang, L.; Liu, X. M.; Liang, Y. Q.; Cui, Z. D.; Yang, X. J.; Zhu, S. L.; Li, Z. Y.; Zheng, Y. F.; Yeung, K. W. K.; Wu, S.; Wu, S. L. The effects of a phytic acid/calcium ion conversion coating on the corrosion behavior and osteoinductivity of a magnesium-strontium alloy. *Appl. Surf. Sci.* **2019**, *484*, 511−523.
(31) Kalaiyarasan, M.; Pugalmani, S.; Rajendran, N. Fabrication of chitosan/silica hybrid coating on AZ31 Mg alloy for orthopaedic applications. *J. Magnesium Alloys* **2023**, *11*, 614−628.
(32) Zhou, P.; Yu, B. X.; Hou, Y. J.; Duan, G. Q.; Yang, L. X.; Zhang, B.; Zhang, T.; Wang, F. H. Revisiting the cracking of chemical conversion coating on magnesium alloys. *Corros. Sci.* **2021**, *178*, 109069.
(33) Song, E. H.; Cho, K. I.; Kim, H. E.; Jeong, S. H. Biomimetic coating of hydroxyapatite on glycerol phosphate-conjugated polyurethane via mineralization. *ACS Omega* **2017**, *2*, 981−987.
(34) Zang, L.; Chen, Y.; Wu, Y.; Zheng, Y.; Chen, H.; You, D.; Li, L.; Li, J. Comparative tribological and friction behaviors of oil-lubricated manganese phosphate conversion coatings with different crystal sizes on AISI 52100 steel. *Wear* **2020**, *458*−*459*, 203427.
(35) Park, S. S.; Farwa, U.; Park, I.; Moon, B. G.; Im, S. B.; Lee, B. T. In-vivo bone remodeling potential of Sr-d-Ca-P/PLLA-HAp coated biodegradable ZK60 alloy bone plate. *Mater. Today Bio* **2023**, *18*, 100533.
(36) Chen, X. B.; Zhou, X.; Abbott, T. B.; Easton, M. A.; Birbilis, N. Double-layered manganese phosphate conversion coating on magnesium alloy AZ91D: Insights into coating formation, growth and corrosion resistance. *Surf. Coat. Technol.* **2013**, *217*, 147−155.
(37) Cui, X. J.; Liu, C. H.; Yang, R. S.; Fu, Q. S.; Lin, X. Z.; Gong, M. Duplex-layered manganese phosphate conversion coating on AZ31 Mg alloy and its initial formation mechanism. *Corros. Sci.* **2013**, *76*, 474−485.
(38) Bakhsheshi-Rad, H. R.; Hamzah, E.; Ismail, A. F.; Aziz, M.; Daroonparvar, M.; Saebnoori, E.; Chami, A. vitro degradation behavior, antibacterial activity and cytotoxicity of TiO_2-MAO/ZnHA composite coating on Mg alloy for orthopedic implants. *Surf. Coat. Technol.* **2018**, *334*, 450−460.
(39) Ren, M. G.; Cai, S.; Liu, T. L.; Huang, K.; Wang, X. X.; Zhao, H.; Niu, S. X.; Zhang, R. Y.; Wu, X. D. Calcium phosphate glass/MgF_2 double layered composite coating for improving the corrosion resistance of magnesium alloy. *J. Alloys Compd.* **2014**, *591*, 34−40.
(40) Liu, X.; Yue, Z. L.; Romeo, T.; Weber, J.; Scheuermann, T.; Moulton, S.; Wallace, G. Biofunctionalized anti-corrosive silane coatings for magnesium alloys. *Acta Biomater.* **2013**, *9*, 8671−8677.
(41) Plueddemann, E. P. *Silane Coupling Agents*; Springer: Berlin, 1991.
(42) van Ooij, W. J.; Zhu, D. Q.; Prasad, G.; Jayaseelan, S.; Fu, Y.; Teredesai, N. Silane based chromate replacements for corrosion control, paint adhesion, and rubber bonding. *Surf. Eng.* **2000**, *16*, 386−396.
(43) Zuo, K.; Wang, X.; Liu, W.; Zhao, Y. Preparation and characterization of Ce-silane-ZrO_2 composite coatings on 1060 aluminum. *Trans. Nonferrous Met. Soc. China* **2014**, *24*, 1474−1480.
(44) Lai, D. L.; Kong, G.; Miao, X. R.; Che, C. S. Effect of Silane Coating on the Corrosion Resistance of TiO_2 Conversion Films. *Int. J. Electrochem. Sci.* **2018**, *13*, 4055−4070.
(45) Najibzad, A. S.; Amini, R.; Rostami, M.; Kardar, P.; Fedel, M. Active corrosion performance of magnesium by silane coatings reinforced with polyaniline/praseodymium. *Prog. Org. Coat.* **2020**, *140*, 105504.
(46) Lei, L.; Wang, X.; Liu, W.; Tang, Q. W. Surface evaluation and electrochemical behavior of cerium conversion coating modified with silane on magnesium alloy. *Surf. Interface Anal.* **2015**, *47*, 466−473.
(47) Dong, Q. S.; Dai, J. W.; Qian, K.; Liu, H.; Zhou, X. X.; Yao, Q. Q.; Lu, M. M.; Chu, C. L.; Xue, F.; Bai, J. Dual self-healing inorganic-organic hybrid coating on biomedical Mg. *Corros. Sci.* **2022**, *200*, 110230.
(48) Wang, X. J.; Chen, Z. N.; Ren, J.; Kang, H. J.; Guo, E. Y.; Li, J. H.; Wang, T. M. Corrosion behavior of as-cast Mg-5Sn based alloys with in additions in 3.5 wt% NaCl solution. *Corros. Sci.* **2020**, *164*, 108318.
(49) Manzur, J.; Akhtar, M.; Aizaz, A.; Ahmad, K.; Yasir, M.; Minhas, B. Z.; Avcu, E.; Ur Rehman, M. A. Electrophoretic deposition, microstructure, and selected properties of poly(lactic-*co*-glycolic) acid-based antibacterial coatings on Mg substrate. *ACS Omega* **2023**, *8*, 18074−18089.

https://doi.org/10.1021/acsomega.3c02824
ACS Omega 2023, 8, 29374−29387

(50) Wang, S. H.; Liu, C. S.; Yu, H. Y. Research of silane film cooperation with ZrO_2 on electrogalvanized steel. *Acta Metall. Sin.* **2012**, *25*, 480−486.
(51) Dreyer, D. R.; Park, S.; Bielawski, C. W.; Ruoff, R. S. The chemistry of graphene oxide. *Chem. Soc. Rev.* **2010**, *39*, 228−240.
(52) Dalmoro, V.; Azambuja, D. S.; Alemán, C.; Armelin, E. Hybrid organophosphonic-silane coating for corrosion protection of magnesium alloy AZ91: The influence of acid and alkali pre-treatments. *Surf. Coat. Technol.* **2019**, *357*, 728−739.
(53) Feng, M. C.; Fu, Q. Y.; Li, J.; Li, J. Y.; Wang, Q.; Liu, X. N.; Jin, W. H.; Li, W.; Chu, P. K.; Yu, Z. T. Sodium alginate coating on biodegradable high-purity magnesium with a hydroxide/silane transition layer for corrosion retardation. *Colloids Surf. A Physicochem. Eng. Asp.* **2022**, *642*, 128647.
(54) Liu, J.; Liu, H. H.; Yang, X. Y.; Jia, X. P.; Cai, M. F.; Bao, Y. C. Preparation of Si−Mn/biochar composite and discussions about characterizations, advances in application and adsorption mechanisms. *Chemosphere* **2021**, *281*, 130946.
(55) Zhang, H. H.; Liu, Y. W.; Bian, H.; Zhang, Y.; Yang, Z. N.; Zhang, Z.; Chen, Y. Electrodeposition of silane/reduced graphene oxide nanocomposite on AA2024-T3 alloy with enhanced corrosion protection, chemical and mechanical stability. *J. Alloys Compd.* **2022**, *911*, 165058.
(56) Shanmugam, S.; Ravichandran, K.; Sankara Narayanan, T. S. N.; Lee, M. H. A facile electrochemical approach for the deposition of iron-manganese phosphate composite coatings on aluminium. *RSC Adv.* **2015**, *5*, 988−1008.
(57) Zhu, D. Q.; van Ooij, W. J. Corrosion protection of metals by water-based silane mixtures of bis-[trimethoxysilylpropyl]amine and vinyltriacetoxysilane. *Prog. Org. Coat.* **2004**, *49*, 42−53.
(58) Shi, Z. M.; Liu, M.; Atrens, A. Measurement of the corrosion rate of magnesium alloys using Tafel extrapolation. *Corros. Sci.* **2010**, *52*, 579−588.
(59) Zhang, H.; Luo, R. F.; Li, W. J.; Wang, J.; Maitz, M. F.; Wang, J.; Wan, G. J.; Chen, Y. Q.; Sun, H.; Jiang, C. X.; Shen, R.; Huang, N. Epigallocatechin gallate (EGCG) induced chemical conversion coatings for corrosion protection of biomedical MgZnMn alloys. *Corros. Sci.* **2015**, *94*, 305−315.
(60) Popova, A.; Sokolova, E.; Raicheva, S.; Christov, M. AC and DC study of the temperature effect on mild steel corrosion in acid media in the presence of benzimidazole derivatives. *Corros. Sci.* **2003**, *45*, 33−58.
(61) John, S.; Joseph, B.; Aravindakshan, K. K.; Joseph, A. Inhibition of mild steel corrosion in 1 M hydrochloric acid by 4-(N, N-dimethylaminobenzilidine)-3-mercapto-6-methyl-1,2,4-triazin(4H)-5-one (DAMMT). *Mater. Chem. Phys.* **2010**, *122*, 374−379.
(62) Daroonparvar, M.; Yajid, M. A. M.; Yusof, N. M.; Bakhsheshi-Rad, H. R.; Hamzah, E.; Kamali, H. A. Microstructural characterization and corrosion resistance evaluation of nanostructured Al and Al/AlCr coated Mg-Zn-Ce-La alloy. *J. Alloys Compd.* **2014**, *615*, 657−671.
(63) Fu, L. H.; Dong, C. F.; Li, X. G.; Han, W. Electrochemical behaviors of magnesium alloy with phosphate conversion coating in NaCl solutions. *Rare Met.* **2016**, *35*, 747−757.

https://doi.org/10.1021/acsomega.3c02824
ACS Omega 2023, 8, 29374−29387